Optics Letters

Coexistence of cavity solitons with different polarization states and different power peaks in all-fiber resonators

Etienne Averlant,[1,2,*] Mustapha Tlidi,[1] Krassimir Panajotov,[2,3] and Lionel Weicker[4,5]

[1]Faculté des Sciences, Université libre de Bruxelles (ULB), Boulevard du triomphe, 1050 Brussels, Belgium
[2]Vrije Universiteit Brussel, Department of Applied Physics and Photonics, Brussels Photonics (B-PHOT), Pleinlaan 2, B-1050 Brussels, Belgium
[3]Institute of Solid State Physics, Bulgarian Academy of Sciences, 72 Tzarigradsko Chaussee Boulevard, 1784 Sofia, Bulgaria
[4]Chair in Photonics, LMOPS, CentraleSupélec, Université Paris-Saclay, F-57070 Metz, France
[5]Chair in Photonics, LMOPS, CentraleSupélec, Université de Lorraine, F-57070 Metz, France
*Corresponding author: eaverlan@ulb.ac.be

We theoretically investigate a weakly birefringent all-fiber cavity subject to linearly polarized optical injection. We describe the propagation of light inside the cavity using, for each linear polarization component of the electric field, the Lugiato–Lefever model. These two components are coupled by cross-phase modulation. We show that, for a wide range of parameters, there is a coexistence between a homogeneous steady state and two different types of temporal vector cavity solitons, which can be hosted in the same system. They differ by their polarization state and peak intensity. We construct their bifurcation diagram and show that they are connected through a saddle-node bifurcation. Finally, we show that vector cavity solitons exhibit multistability involving different polarization states with different energies. © 2017 Optical Society of America

Driven optical cavities filled with Kerr media are basic configurations in nonlinear optics. They support temporal cavity solitons (CSs) in the form of short optical pulses propagating along the cavity. They are also called localized structures and have been theoretically predicted in Ref. [1] and experimentally observed in Ref. [2]. They arise due to modulation instability (MI) [3]. The best-known types of MIs are Benjamin–Feir [4], Faraday [5], and Turing [6] instabilities. Other types of instabilities giving rise to pulse trains include the dissipative parametric instability [7] and vector resonance multimode instability [8]. The formation of CSs and their connections to optical comb generation have been established [9,10].

Today, there is an increasing interest in the polarization properties of CSs. Vector CSs have a nontrivial polarization state. Fiber cavities have been shown to be able to host two types of vector CSs: (i) group velocity-locked vector solitons (GVLVS) [11,12], where the polarization degree of freedom allows vector CSs to have an evolving polarization state, drawing orbits on the Poincaré sphere, and (ii) polarization locked vector soliton (PLVS), where the CS preserves its polarization state under the effect of birefringence. PLVSs have been theoretically predicted by Akhmediev [13] and experimentally observed in Refs. [14–16]. Both GVLVS and PLVS can be generated in fiber-laser-based devices [17].

In this Letter, we theoretically show the existence of different PLVSs in a weakly birefringent all-fiber cavity. The resulting vector CSs do not only differ by their polarization state, but also by the energy they carry. In addition, we show that these two different types of vector CSs can coexist for the same fixed parameter values. We show also that they are connected through a saddle-node bifurcation. Finally, we numerically construct their bifurcation diagram.

We consider a weakly birefringent optical fiber cavity submitted to coherent optical pumping, and place ourselves in a power regime where Brillouin and Raman scatterings are neglectable. In that framework, the propagation of light inside the cavity is governed by the following set of coupled nonlinear Schrödinger equations, written in a reference frame moving with the group velocity of the light:

$$\frac{\partial A_{x,y}}{\partial z} + ik_0'' \frac{\partial^2 A_{x,y}}{\partial \tau^2}$$
$$= i\gamma \left[\left(|A_{x,y}|^2 + \frac{2|A_{y,x}|^2}{3} \right) A_{x,y} + \frac{A_{x,y}^* A_{y,x}^2 e^{\mp 2i\Delta\beta z}}{3} \right]. \quad (1)$$

In these equations, A_x (A_y) is the slowly varying electric field envelope polarized along the slow (fast) axis of the birefringent fiber. A_x^* and A_y^* are their complex conjugates. z is the longitudinal coordinate. k_0'' is the second-order dispersion coefficient, and γ is a nonlinear term that accounts for the Kerr effect, crossed-phase modulation, and four-wave mixing. $\Delta\beta$ corresponds to the wavenumber mismatch between the two

orthogonal polarization components, and is defined as $\Delta\beta = 2\pi|n_x - n_y|/\lambda$.

Integration of the propagation equations over the length of the ring cavity L yields

$$A_{x,y}(L,\tau) - A_{x,y}(0,\tau) = L\left[-ik_0''\frac{\partial^2 A_{x,y}}{\partial\tau^2} - \alpha A_{x,y}\right.$$

$$\left. + i\gamma\left(|A_{x,y}|^2 + \frac{2|A_{y,x}|^2}{3}\right)A_{x,y}\right] \pm \frac{\gamma A_{x,y}^* A_{y,x}^2(1 - e^{\mp 2i\Delta\beta L})}{6\Delta\beta}.$$

A typical cavity length for CS generation is roughly 400 m long [2], while weakly birefringent fibers have $\Delta\beta \approx 1 \text{ m}^{-1}$ [18], which means that there is a difference of at least two orders of magnitude between the Kerr crossed-phase modulation terms, and the four-wave mixing term. We therefore neglect four-wave mixing for the rest of this communication.

The light circulating within the cavity further undergoes coherent superposition with the input field at the coupling beam splitter. This is described by the following cavity boundary conditions, connecting the slowly varying amplitudes of the light after n passes $A_{x,y,n}$ with those after $n + 1$ passes:

$$A_{x,y,n+1}(0,\tau) = TA_{Ix,y} + Re^{-i\delta_{x,y}}A_{x,y,n}(L,\tau). \quad \textbf{(2)}$$

T and R are the transmission and reflexion coefficients at the coupling beam splitter, $A_{Ix,y}$ are the linear components of the optical injection along the slow and fast axes of the birefringent fiber, and the coefficients $\delta_{x,y}$ account for the phase difference between the injection field and the light that propagated over the whole length of the fiber.

Equations (1) and (2) constitute an infinite dimensional map that can be simplified using a mean field approximation. To do so, we further assume a high-finesse cavity $T \ll 1$. We further assume $\delta_{x,y} \ll 1 \gg \gamma L|A_{x,y}|^2$. We also set the second-order dispersion characteristic length to be much longer than the cavity size. The last step of the derivation of the model consists of introducing the continuous limit as $[A_{n+1}(z=0) - A_n(z=0)]/t_r = \partial A/\partial t'$, where t_r is the cavity round-trip time. Under these approximations, the vectorial Lugiato-Lefever model reads

$$\frac{\partial E_x}{\partial t} = E_I \cos(\Psi) - (1 + i\theta_x)E_x$$

$$+ i\left(|E_x|^2 + \frac{2|E_y|^2}{3}\right)E_x + i\beta_2\frac{\partial^2 E_x}{\partial\tau^2}, \quad \textbf{(3a)}$$

$$\frac{\partial E_y}{\partial t} = E_I \sin(\Psi) - (1 + i\theta_y)E_y$$

$$+ i\left(|E_y|^2 + \frac{2|E_x|^2}{3}\right)E_y + i\beta_2\frac{\partial^2 E_y}{\partial\tau^2}. \quad \textbf{(3b)}$$

Here, $E_{x,y}$ are the slowly varying electric field envelopes polarized in the slow and fast axis, respectively. The holding beam E_I is real and positive to fix the origin of the phase, with Ψ its linear polarization direction with respect to slow-axis orientation. The detunings between the frequency of the holding beam and the cavity resonances for each polarization direction are θ_x and θ_y. The second-order chromatic dispersion coefficient is β_2, considered to be the same for slow- and fast-axis polarization directions. The time t is the slow time, which is proportional to round-trip time. It describes the evolution of field envelope from one cavity round-trip to another. The fast

time τ places us in the moving frame with the group velocity of the light propagating in the cavity. These quantities are related to the physical variables via the renormalizations $t = t'T^2/2t_r$, $E_{Ix,y} = 2\sqrt{\gamma}A_{Ix,y}/T$, $\theta_{x,y} = 2\delta_{x,y}/T^2$, $\beta_2 = -2Lk_0''/T^2$, and $E_{x,y} = \sqrt{\gamma}A_{x,y}$. Note that a similar model has been described in Ref. [19].

The homogeneous steady states (HSSs) satisfying $\partial^2 E_{x,y}/\partial\tau^2 = \partial E_{x,y}/\partial t$ of Eq. (3b) in terms of a total intensity $|E|^2 = |E_x|^2 + |E_y|^2$ as a function of the injected field amplitude E_I are plotted in Fig. 1 for three different values of the detuning parameter θ_x. Three branches of solutions corresponding to the positive slope are stable ($\partial|E|^2/\partial E_I > 0$). The red curves with a negative slope ($\partial|E|^2/\partial E_I < 0$) are plane-wave unstable. From Fig. 1, we see that when increasing θ_x, the width of the hysteresis loop involving two stable HSSs (delimited by the limit points C and D) decreases. The bistable regions A–B and C–D move to higher and lower injection strengths, respectively. However, when performing a standard linear stability analysis of the HSSs with respect to finite frequency perturbation of the form $\exp(i\omega\tau + \sigma t)$, the upper branches (in blue) are modulationally unstable.

A summary of the linear stability analysis is provided in the parameters plane (E_I, θ_x) of Fig. 2. The black and blue (dark gray) regions correspond to areas in which the system admits a stable HSS and a MI unstable state, respectively. Green (light gray) represents the coexistence of a stable HSS and a MI unstable state, and red (gray) the coexistence of two MI unstable states. Finally, the white area represents the coexistence of a stable HSS and two MI unstable states.

Polarization instability in an optically injected isotropic nonlinear cavity has been considered already in 1994 in
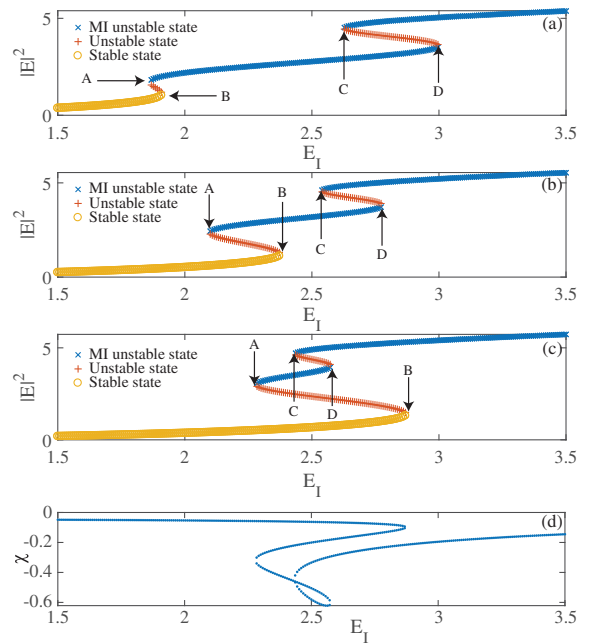

Fig. 1. (a)–(c) Intracavity field intensity as a function of E_I. Red + denotes linearly unstable states, yellow ° denotes linearly stable states, and blue × denotes MI unstable states. A and B denote the lower and higher limits of the first hysteresis, whereas C and D denote the lower and higher limits of the second hysteresis. (d) Ellipticity of the different HSSs as a function of the optical injection field. Parameters are $\beta_2 = 1$, $\psi = \pi/4$, $\theta_y = 4.3$, $\theta_x = 2$ (a), $\theta_x = 2.5$(b), and $\theta_x = 3$ (c and d).
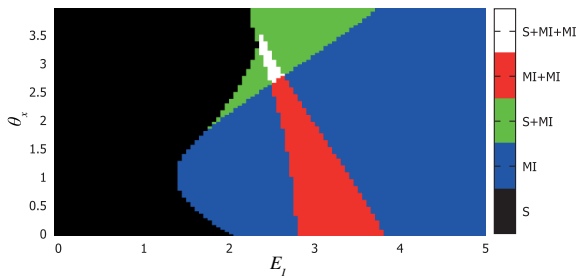
Fig. 2. Stability map of the HSSs in the parameter plane (E_I, θ_x). Black color corresponds to the region where the system allows a single stable state, blue (dark gray) to a single MI unstable state, green (light gray) to the coexistence of a stable state and a MI unstable state, red (gray) to the coexistence of two MI unstable states, and white to the coexistence of a stable state with two MI unstable states. The map has been obtained from a linear stability analysis of Eq. (3b). Parameters are the same as in Fig. 1.

Ref. [20]. For a linearly polarized optical injection, a pitchfork bifurcation between two circularly polarized branches of different handednesses has been found, and MI regions for both normal and anomalous dispersion regime have been determined. In our case, the cavity is weakly birefringent, and polarization multistability is observed between branches with different ellipticities, as illustrated in Fig. 1(d). Moreover, in Ref. [20] no CS operation has been considered. We show below that polarization multistability gives rise to a coexistence of PLVSs with different elliptical polarization states. Coexistence of MI of modes with different transverse profiles in the form of a mixed mode in a whispering-gallery-mode resonator has been demonstrated in Ref. [21].

When a stable HSS and a periodic train of pulses coexist due the subcritical nature of MI bifurcations, it is often possible to generate cavity solitons in a finite range of parameters called a pinning zone. This mechanism has been established for the scalar Lugiato–Lefever equation in Ref. [1]. When the polarization degree of freedom is taken into account, there are two different MI patterns coexisting with a stable state, as indicated in the white area of the map (cf. Fig. 2). We hence can expect that the system can generate two kinds of CSs for the values of parameters in the white area. Indeed, the numerical simulation of Eq. (3b) with periodic boundary conditions along the τ coordinate reveals the occurrence of two types of CSs, as shown in Fig. 3. They are presented as a function of the Stokes parameters, defined as $S_0 = |E_x|^2 + |E_y|^2$, $S_1 = |E_x|^2 - |E_y|^2$, $S_2 = E_x^* E_y + E_x E_y^*$, $S_3 = i(E_x^* E_y - E_x E_y^*)$. The initial condition used is that of a homogeneous background on which two hard perturbations with different polarization properties have been added in the vicinity of $\tau = 8$ and $\tau = 30$. As can be seen from Fig. 3, there are three distinct regions around $\tau = 8$ and $\tau = 30$: two CSs labelled A and B, and, in between the background. The CS labelled A has the higher intensity (S_0 parameter), and hence corresponds to the brightest pulse. Next to its maximum value is represented its polarization state, which is an ellipse. The parameters of this ellipse have been calculated at the maximum value of S_0. Two other ellipses have been drawn on this graph. The lower (unmarked) one represents the polarization state of the background, whereas B corresponds to the maximum of the second CS. The difference between their polarization states can be evidenced by looking at their
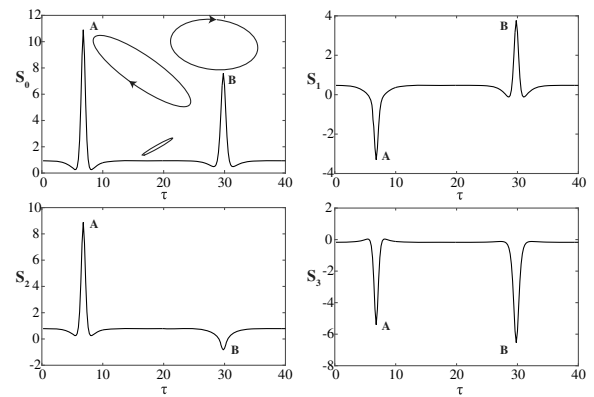
Fig. 3. Numerical simulation of Eq. (3b) after 500 units of time, expressed as a function of the Stokes parameters of the output field. On the upper-left plot (S_0), LSs and the background have been marked with their respective polarization ellipses. The τ step has been fixed at 0.2, the time step has been fixed to 0.01. The τ integration has been performed using a second-order finite difference method, whereas the time integration has been performed using a Runge–Kutta method of order 4. Parameters are $E_I = 2.54$, $\theta_x = 2.75$, $\beta_2 = 1$, $\theta_y = 4.3$, and $\Psi = \pi/4$.

Stokes parameters: at its maximum intensity, CS A has a negative S_1 and a positive S_2, whereas CS B has a positive S_1 and a negative S_2. Both of these structures have a large negative S_3 (slightly different between CSs A and B). This indicates a large right-handed circular component. The fact that their polarization states differ distinguishes these structures from the ones presented in Ref. [22]. Indeed, in this work, the authors observed a tristability that arises from a multivalued stationary state for an Ikeda map. However, this dynamic is not captured by the scalar Lugiato–Lefever model. They do not consider the polarization degree of freedom.

We are interested in the situation where two stable CSs solutions coexist with different polarization and different peak intensities and can connect to each other. We fix the detuning parameters and we vary the amplitude of the injected field. Two CS solutions with different intensity peaks and different polarization states are generated as shown in Figs. 4(a) and 4(b). For $E_{I0} < E_I < E_{I1}$, only the CS with smaller intensity is stable, as shown in Fig. 4(c). In this figure, we plot the "energy" or normalized number of photons $N_0 = \int_{t_r} (|E|^2 - |E_0|^2) d\tau$ as a function of E_i with $|E_0|^2$ being the HSS intensity. In this regime, an unstable branch of CSs of type B emerges from the HSSs (dashed curve), and at the turning point $E_I = E_{I0}$ it becomes stable (continuous curve). These solutions are found by using appropriate initial conditions and are then continued in parameter space using the Newton method. Periodic boundary conditions are used. When increasing the injected field amplitude, the CS of type B is stable until it reaches the saddle-node bifurcation at $E_I = E_{I2}$, where the slope becomes infinite. Afterwards, by decreasing E_i, the CS type B begins to grow, and transition to CS of type A occurs through an unstable branch (dotted line). The two types of CSs are connected through double saddle-node bifurcation. There is then a finite domain of the injected field $E_{I1} < E_I < E_{I2}$, where the intracavity field exhibits a bistable behavior between the two types of CSs, as shown in Fig. 4(c). When increasing the injected field amplitude $E_I > E_{I2}$, only the CS of large intensity survives.
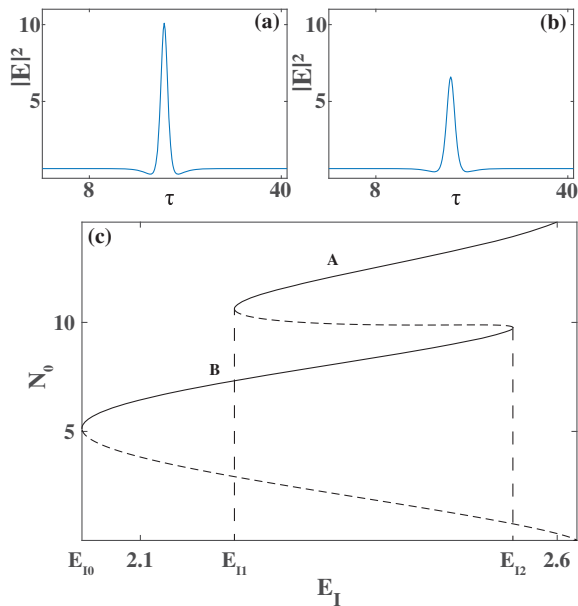
Fig. 4. (a) Profile of a CS of type A. (b) Profile of a CS of type B. (c) Evolution of the N_0 quantity associated with the transition from a constant background to a structure of type A, via a structure of type B. Numerical simulations have been performed with the same parameters as in Fig. 3.

The intracavity field can host more than two types of CSs. The system exhibits a high degree of multistability, and the bifurcation diagram becomes complex. An example of three-peak solutions involving either type A or B or a mixed CS solution is shown in Fig. 5. In this figure, the evolution of the "energy" or normalized number of photons $N = \int_{t_r} |E|^2 d\tau$ is plotted as a function of E_I. Insets represent the profile of the different branches, with an arrow pointing to the corresponding branch.
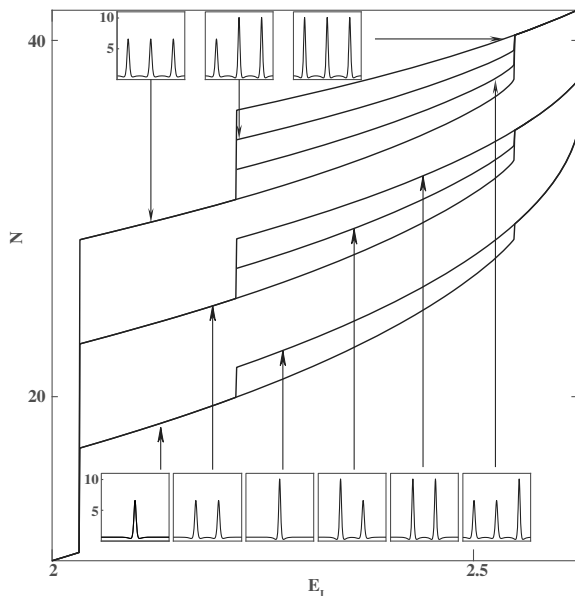
Fig. 5. Evolution of the quantity N (see text) as a function of E_I. A step of 0.001 has been used for E_I. Each numerical simulation has been performed using 256 cells, with a τ step of 0.1 and a t step of 0.001, for a total time of 100 units.

As can be seen from this figure, our system not only displays stable branches corresponding to CSs of type A and B, but also mixed states containing structures of both types.

To conclude, we have investigated a weakly birefringent fiber cavity subject to linearly polarized optical pumping. The mean field approach has been used, leading to two coupled Lugiato–Lefever models. A linear stability analysis has shown that there exists a parameter domain in which two MI branches coexist with a HSS. Numerical simulations of the vectorial Lugiato–Lefever model have shown the existence of two stable cavity solitons having different Stokes parameters, i.e., different polarization properties, and different peak intensities. We have characterized their formation by drawing their bifurcation diagram. Numerical simulations involving several peaks have shown the larger complexity of the bifurcation diagram.

REFERENCES

1. A. J. Scroggie, W. J. Firth, G. S. McDonald, M. Tlidi, R. Lefever, and L. A. Lugiato, Chaos Solitons Fractals **4**, 1323 (1994).
2. F. Leo, S. Coen, P. Kockaert, S.-P. Gorza, P. Emplit, and M. Haelterman, Nat. Photonics **4**, 471 (2010).
3. M. Tlidi, K. Staliunas, K. Panajotov, A. G. Vladimirov, and M. G. Clerc, Philos. Trans. R. Soc. A **372**, 20140101 (2014).
4. T. B. Benjamin and J. E. Feir, J. Fluid Mech. **27**, 417 (1967).
5. M. Faraday, Philos. Trans. R. Soc. London **121**, 299 (1831).
6. A. M. Turing, Philos. Trans. R. Soc. B **237**, 37 (1952).
7. A. M. Perego, N. Tarasov, D. V. Churkin, S. K. Turitsyn, and K. Staliunas, Phys. Rev. Lett. **116**, 028701 (2016).
8. S. V. Sergeyev, H. Kbashi, N. Tarasov, Y. Loiko, and S. A. Kolpakov, Phys. Rev. Lett. **118**, 033904 (2017).
9. S. Coen, H. G. Randle, T. Sylvestre, and M. Erkintalo, Opt. Lett. **38**, 37 (2013).
10. T. Herr, V. Brasch, J. D. Jost, C. Y. Wang, N. M. Kondratiev, M. L. Gorodetsky, and T. J. Kippenberg, Nat. Photonics **8**, 145 (2014).
11. S. V. Sergeyev, C. Mou, E. G. Turitsyna, A. Rozhin, S. K. Turitsyn, and K. Blow, Light Sci. Appl. **3**, e131 (2014).
12. C. Mou, S. Sergeyev, A. Rozhin, and S. Turitsyn, Opt. Lett. **36**, 3831 (2011).
13. N. Akhmediev, A. Buryak, and J. Soto-Crespo, Opt. Commun. **112**, 278 (1994).
14. S. T. Cundiff, B. C. Collings, N. N. Akhmediev, J. M. Soto-Crespo, K. Bergman, and W. H. Knox, Phys. Rev. Lett. **82**, 3988 (1999).
15. B. C. Collings, S. T. Cundiff, N. N. Akhmediev, J. M. Soto-Crespo, K. Bergman, and W. H. Knox, J. Opt. Soc. Am. B **17**, 354 (2000).
16. J. M. Soto-Crespo, N. N. Akhmediev, B. C. Collings, S. T. Cundiff, K. Bergman, and W. H. Knox, J. Opt. Soc. Am. B **17**, 366 (2000).
17. H. Zhang, D. Y. Tang, L. M. Zhao, X. Wu, and H. Tam, Opt. Express **17**, 455 (2009).
18. G. P. Agrawal, *Nonlinear Fiber Optics*, 4th ed., Optics and Photonics (Academic, 2006).
19. M. Hoyuelos, P. Colet, M. San Miguel, and D. Walgraef, Phys. Rev. E **58**, 2992 (1998).
20. M. Haelterman, S. Trillo, and S. Wabnitz, J. Opt. Soc. Am. B **11**, 446 (1994).
21. G. D'Aguanno and C. R. Menyuk, Phys. Rev. A **93**, 043820 (2016).
22. T. Hansson and S. Wabnitz, J. Opt. Soc. Am. B **32**, 1259 (2015).